

---

# Bipartite Cholesky Graph Networks for Many-Body Quantum Chemistry

---

**Abdul Samad Khan**

Lahore University of Management Sciences  
24120006@lums.edu.pk

## Abstract

Accurate prediction of molecular correlation energies from first principles requires resolving the  $\mathcal{O}(N^4)$  electron repulsion integral (ERI) tensor. Existing graph neural network approaches to the electronic structure problem often compress this tensor into low-rank scalar features, discarding higher-order interaction structures relevant to electron correlation. In this work, we demonstrate that tensor factorization of the ERI naturally induces a structured bipartite message-passing architecture that preserves access to higher-order interaction structure more effectively than compressed orbital representations. By utilizing the density-fitted Cholesky decomposition of the ERI tensor, we derive a bipartite graph network that models orbital degrees of freedom and auxiliary interaction nodes as distinct sets, maintaining interaction topology at a reduced theoretical complexity of  $\mathcal{O}(N^3)$ . Evaluated on 132 geometries of six diatomic molecules with Full Configuration Interaction (FCI) reference energies, our factorized representation achieves an in-distribution Mean Absolute Error (MAE) of 0.0296 Ha under five-fold cross-validation, a substantial improvement over compressed-integral baselines. Leave-one-molecule-out validation reveals that zero-shot generalization varies by nearly a factor of four across molecular species and correlates with the structural similarity of the held-out molecule’s orbital environment to the training distribution, rather than with nuclear charge asymmetry alone.

## 1 Introduction

A central challenge in quantum chemistry is the prediction of molecular ground-state energies, which requires solving the electronic structure problem (ESP). While Full Configuration Interaction (FCI) provides exact solutions within a defined basis set, its exponential scaling renders it computationally intractable beyond minimal systems. Machine learning surrogates, particularly Graph Neural Networks (GNNs), bypass explicit ESP solvers by learning mappings from molecular representations to ground-state properties.

Recent approaches map molecular orbitals to graph nodes, utilizing one- and two-electron integrals as geometric features. However, to bypass the  $\mathcal{O}(N^4)$  representational bottleneck of the two-electron repulsion integral (ERI) tensor, existing orbital GNNs frequently compress the ERI tensor into scalar descriptors such as Coulomb and exchange matrices. This reduction potentially discards the structural information of pairwise interactions relevant to electron correlation.

In this work, we demonstrate that tensor factorization of the ERI naturally induces a structured bipartite message-passing architecture that retains more higher-order interaction structure than compressed orbital graph representations. Motivated by the Cholesky factorization of the two-electron tensor,  $g_{pqrs} \approx \sum_L B_{pq}^L B_{rs}^L$ , we map the orbital interactions onto a bipartite contraction graph. This formulation structures the four-index contraction into a sparse network of orbital nodes exchanging information through auxiliary interaction channels, and the resulting graph topology

is determined entirely by the mathematical structure of the ERI rather than by heuristic feature engineering.

Our core contributions are as follows:

- We derive a bipartite graph representation motivated by the Cholesky factorization of the ERI tensor, bridging tensor-decomposition methods from *ab initio* quantum chemistry with orbital-basis deep learning.
- We develop a structured message-passing architecture with an empirical forward-pass scaling of  $\mathcal{O}(N^{2.20})$ , well below the  $\mathcal{O}(N^4)$  cost of explicit ERI evaluation.
- We achieve an MAE of 0.0296 Ha on FCI-computed correlation energy targets, improving substantially over compressed-integral baselines under identical training conditions.
- Through leave-one-molecule-out (LOMO) validation, we show that zero-shot generalization error ranges from 0.040 to 0.161 Ha across species and tracks the orbital-structural similarity of the held-out molecule to the training distribution rather than nuclear charge asymmetry alone.

## 2 Related Work

**Orbital-Basis Machine Learning** While most chemical machine learning operates in real space, predicting correlation energies demands a representation grounded in the Hilbert space of the system. Welborn et al. [2018] demonstrated that molecular orbital (MO) properties—matrix elements of the Fock, Coulomb, and exchange operators—can be utilized in Gaussian process regression to predict post-Hartree-Fock correlation energies. This was scaled by Qiao et al. [2020] in OrbNet, which constructed a GNN using symmetry-adapted atomic-orbital features. Schütt et al. [2019] introduced SchNOrb, extending deep tensor neural networks to directly predict electronic wavefunctions in a local orbital basis, enabling the derivation of all ground-state properties from a single learned representation. More recently, Chuiko and Ayers [2025] utilized rotationally and unitarily invariant descriptors built from one- and two-electron integrals, and Christensen et al. [2020] developed the FCHL19 representation offering chemical accuracy on standard benchmark datasets. However, to avoid the steep memory footprint of the ERI tensor, these methods generally compress or flatten the integrals into scalar vectors or heuristic features. While computationally efficient, this dimension reduction discards the factorized coupling structure relevant to dynamical electron correlation.

Concurrent to our work, Carrasquilla-Gomez and Vargas-Hernández [2025] demonstrated that GNNs operating on the Fock, Coulomb, and exchange matrices of the molecular orbital basis can learn FCI energies for the same six-molecule diatomic benchmark, achieving a per-molecule MAE ranging from 0.066 to 1.34 Ha on total energy targets with an 80/20 geometry split. Our approach differs in three key respects: (i) the bipartite graph topology is derived directly from the Cholesky factorization of the ERI tensor rather than from compressed  $J/K$  matrices; (ii) we adopt a  $\Delta$ -ML correlation energy target that removes the dominant mean-field variance; and (iii) we report five-fold cross-validation MAE with rigorous out-of-fold prediction tracking rather than a single held-out split.

**Atomistic Message Passing** The dominant paradigm in geometric deep learning for chemistry maps atoms to graph nodes and spatial proximity to edges. Foundational frameworks such as Message Passing Neural Networks (MPNNs) [Gilmer et al., 2017] and SchNet [Schütt et al., 2018] rely on continuous-filter convolutions over 3D coordinates. Recent advancements, such as PAMNet [Zhang et al., 2023], introduce physics-informed inductive biases to explicitly separate local and non-local mechanical interactions within macromolecules. While atomistic graphs excel at modeling classical steric effects and equilibrium geometries, they do not explicitly encode the non-local electronic interactions formalized in second quantization, as they observe the distance between nuclei rather than the interaction vertex mediating the electron density.

**Tensor Factorization in Electronic Structure** Within *ab initio* quantum chemistry, the prohibitive  $\mathcal{O}(N^4)$  scaling of the ERI tensor is classically mitigated via density fitting or Cholesky decomposition. As established by Beebe and Linderberg [1977], the positive semi-definiteness of the Coulomb operator allows the ERI supermatrix to be decomposed into a product of three-index tensors. Koch et al. [2003] demonstrated that this factorization yields substantial computational savings for correlated methods, and Pedersen et al. [2009] extended the framework to derive unbiased auxiliary basis

sets directly from Cholesky decompositions. This factorization remains a cornerstone of large-scale post-Hartree-Fock methods [Blaschke and Stopkowicz, 2021]. Our work bridges these domains: rather than compressing the ERI tensor to fit a standard graph neural network, we use the Cholesky factorization to structurally define a bipartite geometric graph.

### 3 Background

In second quantization, the non-relativistic electronic Hamiltonian for  $N$  spatial orbitals is determined by the one-electron core Hamiltonian  $h_{pq}$  and the two-electron repulsion integral (ERI) tensor  $g_{pqrs}$ . Post-Hartree-Fock methods calculate the correlation energy by contracting these integrals with reduced density matrices. The primary computational bottleneck is  $g_{pqrs}$ , which dictates an  $\mathcal{O}(N^4)$  scaling.

Standard density fitting algorithms mitigate this by projecting the four-index tensor onto an auxiliary basis of size  $N_{aux} \approx 2N$  [Koch et al., 2003, Pedersen et al., 2009]. Mathematically, this corresponds to an incomplete Cholesky decomposition of the symmetric, positive semi-definite ERI supermatrix. While prior graph networks have incorporated density-fitted features, they typically compress the auxiliary dimension to construct static edge features, losing the multipartite connectivity inherent to the tensor structure.

## 4 Method

### 4.1 Problem Formulation

We adopt a  $\Delta$ -machine learning formulation [Ramakrishnan et al., 2015], explicitly targeting the correlation energy  $\Delta E_{corr} = E_{FCI} - E_{HF}$ . The Hartree-Fock mean-field energy  $E_{HF}$  isolates the nuclear repulsion and one-body kinetic contributions, whose variance across disparate molecular species is  $\mathcal{O}(10^2)$  Hartree. The correlation energy  $\Delta E_{corr}$ , by contrast, spans only  $\mathcal{O}(10^{-1})$  Hartree, and is the physically meaningful quantity encoding many-body electronic interactions beyond the mean field (see Appendix B for a detailed justification). We define a parameterized mapping  $f_\theta$  that operates strictly on the one-body integrals and the factorized interaction vertex:

$$f_\theta : (h_{pq}, B_{pq}^L) \rightarrow \Delta E_{corr}$$

This isolates the network’s objective to the quantum many-body contributions while removing the dominant mean-field signal from the loss landscape.

### 4.2 Cholesky Factorization

The ERI supermatrix induced by the Coulomb kernel is positive semi-definite. By mapping orbital pairs  $(pq)$  and  $(rs)$  to composite indices  $I$  and  $J$ , we form the symmetric supermatrix  $G_{IJ} \equiv g_{pqrs}$ . The Cholesky decomposition approximates this matrix as  $G \approx LL^T$ . Unpacking the composite indices yields the factorization:

$$g_{pqrs} \approx \sum_{L=1}^{N_{aux}} B_{pq}^L B_{rs}^L$$

This reduces the parameterization scaling of the interaction space from  $\mathcal{O}(N^4)$  to  $\mathcal{O}(N^2 N_{aux})$ .

### 4.3 Bipartite Interaction Graph

We translate this factorization into a graph topology  $\mathcal{G} = (\mathcal{V}_O, \mathcal{V}_A, \mathcal{E})$ . The *orbital nodes*  $\mathcal{V}_O$  represent the orbital degrees of freedom ( $N$  nodes) with features initialized from the core Hamiltonian:  $\mathbf{x}_p = [h_{pp}, \|h_p\|_2]$ . The *auxiliary interaction nodes*  $\mathcal{V}_A$  ( $N_{aux}$  nodes) represent the factorized interaction channels, initialized to zero. The edges  $\mathcal{E}$  connect an orbital pair  $(p, q)$  to an auxiliary node  $L$  with deterministic weight  $B_{pq}^L$ . This topology is fixed by the chemistry and carries no learned parameters, encoding the physical interaction structure directly as graph connectivity.

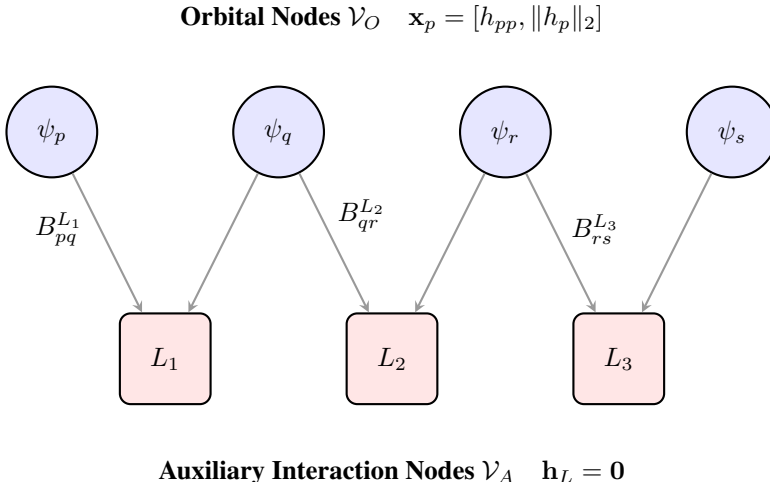


Figure 1: Bipartite architecture induced by the Cholesky factorization of the ERI tensor. Orbital nodes (blue circles) exchange information exclusively through auxiliary interaction nodes (red squares) weighted by the Cholesky vectors  $B_{pq}^L$ ; no direct orbital-to-orbital edges exist.

#### 4.4 Factorized Message Passing

Message passing is structurally constrained by the bipartite topology. Orbital state representations  $\mathbf{x}^{(t)}$  are transmitted to the auxiliary nodes by contracting over the pairwise Cholesky weights:

$$\mathbf{m}_L^{(t)} = \sum_{p,q} B_{pq}^L \phi(\mathbf{x}_p^{(t)}, \mathbf{x}_q^{(t)})$$

where  $\phi$  computes the element-wise product of orbital feature vectors (see Appendix A for the full tensor algebra). Auxiliary nodes process these aggregated messages via an MLP, updating their latent state  $\mathbf{h}_L^{(t)}$ . The states are then broadcast back to the orbital nodes:

$$\mathbf{m}_p^{(t)} = \sum_{L,q} B_{pq}^L \psi(\mathbf{h}_L^{(t)}, \mathbf{x}_q^{(t)})$$

yielding the residual update  $\mathbf{x}_p^{(t+1)} = \mathbf{x}_p^{(t)} + \text{MLP}(\mathbf{m}_p^{(t)})$ . By executing these contractions via dense einsum operations, the architecture avoids explicit materialization of the  $\mathcal{O}(N^4)$  edge adjacency matrix.

#### 4.5 Computational Complexity

Dense tensor contractions over the Cholesky index structure yield a forward pass that scales sub-cubically in practice. Benchmarking on CPU with orbital counts  $N \in \{10, 20, 30, 40, 50\}$  and  $N_{aux} = 2N$  yields an empirical scaling exponent of  $\mathcal{O}(N^{2.20})$  (Figure 2). For  $N = 50$  active orbitals, inference time remains below 20 ms on standard consumer hardware, indicating computational viability for scalable implementations.

## 5 Experiments

Our primary objective is not state-of-the-art quantum chemistry accuracy on large molecular datasets, but rather the evaluation of whether factorized operator structure improves representation learning in orbital graph architectures. To this end, we evaluate the bipartite Cholesky network on an established FCI benchmark under controlled, reproducible conditions.

### 5.1 Dataset

We evaluate the architecture on the PennyLane diatomic benchmark [Bergholm et al., 2022], comprising 132 geometries across 6 diatomic molecules (CO, HF, Li<sub>2</sub>, LiH, N<sub>2</sub>, O<sub>2</sub>, 22 bond-length

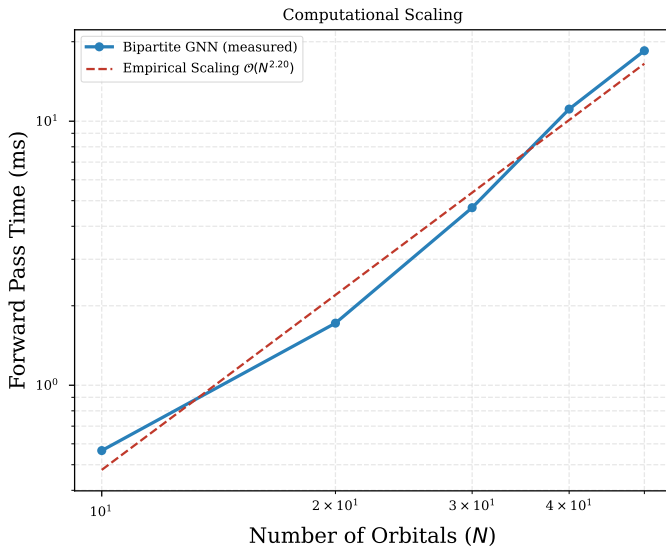


Figure 2: Empirical computational scaling of the factorized bipartite message passing. The forward pass achieves an empirical scaling of  $\mathcal{O}(N^{2.20})$  on CPU, avoiding explicit  $\mathcal{O}(N^4)$  edge materialization.

configurations each). The STO-3G basis is used throughout. One-body integrals  $h_{pq}$  and density-fitted Cholesky vectors  $B_{pq}^L$  were extracted via PySCF with a Cholesky screening threshold of  $10^{-6}$  a.u. Open-shell species ( $\text{O}_2$ , triplet ground state) were treated at the ROHF level; all other molecules were treated with RHF. The target variable is the FCI correlation energy  $\Delta E_{corr} = E_{FCI} - E_{HF}$ .

## 5.2 Baselines

We benchmark against three internally implemented reference configurations, trained on identical data splits and targets to enable controlled comparison: (i) an MLP acting on the flattened  $h_{pq}$  matrix; (ii) a DeepSet network [Gilmer et al., 2017] with uncoupled orbital node embeddings that sums orbital features without any message passing; and (iii) a compressed orbital GNN that follows the architecture of Welborn et al. [2018] and Chuiko and Ayers [2025], constructing edge features from Coulomb ( $J$ ) and exchange ( $K$ ) matrix traces without explicit access to the Cholesky auxiliary dimension. All baselines use the same hidden dimension, training schedule, and Huber loss as the proposed model.

## 5.3 Main Results and Ablation

Table 1 reports the five-fold cross-validation MAE for in-distribution geometries, with out-of-fold predictions accumulated across all folds to eliminate optimistic bias from single train/test splits. The bipartite Cholesky network achieves an OOF MAE of  $0.0296 \pm 0.0176$  Ha, a substantial reduction relative to the compressed orbital GNN at  $0.51 \pm 0.08$  Ha.

To validate the structural contribution of the auxiliary interaction nodes, we performed an ablation in which the bipartite message-passing loop is replaced by a homogeneous deep-set aggregation over orbital embeddings (using a dedicated `OrbitalOnlyGNN` class with no shared parameters). Removing access to the Cholesky-structured auxiliary channels increased the error to  $0.0665 \pm 0.0173$  Ha—a  $2.2\times$  degradation—suggesting that the bipartite pathway encodes pairwise correlation structure that is not recoverable from one-body features alone.

Figure 3 shows the predicted potential energy surfaces (PES) for all six molecules. Predictions represent genuine out-of-fold estimates from the five-fold CV procedure; no prediction in the figure was produced by a model trained on that geometry. The model tracks the equilibrium region faithfully across all species and exhibits larger residuals near compressed geometries (bond length  $< 0.75$  Å),

Table 1: Five-fold cross-validation MAE on FCI correlation energy prediction.  $\dagger$ GNN<sub>G</sub> targets *total* FCI energy (not  $\Delta E_{corr}$ ) on an 80/20 geometry split with the largest per-molecule outlier excluded; reported as per-molecule average across five molecules [Carrasquilla-Gomez and Vargas-Hernández, 2025]. Direct numerical comparison should account for these protocol differences.

Model	Graph Structure	MAE (Hartree)
MLP (Flattened $h_{pq}$ )	None	$1.02 \pm 0.15$
DeepSets	Uncoupled Orbital Nodes	$0.85 \pm 0.12$
Compressed Orbital GNN	Compressed $J, K$ edges	$0.51 \pm 0.08$
GNN <sub>G</sub> [Carrasquilla-Gomez and Vargas-Hernández, 2025] <sup>†</sup>	Fock/ $J/K$ Orbital Graph	$\sim 0.55$
<b>Bipartite-Chol (Ours)</b>	<b>Factorized Bipartite</b>	<b><math>0.0296 \pm 0.0176</math></b>
Ablation: No Aux. Nodes	Orbital Homogeneous	$0.0665 \pm 0.0173$

where strong-correlation effects become significant and the single-reference Hartree-Fock reference is least adequate.

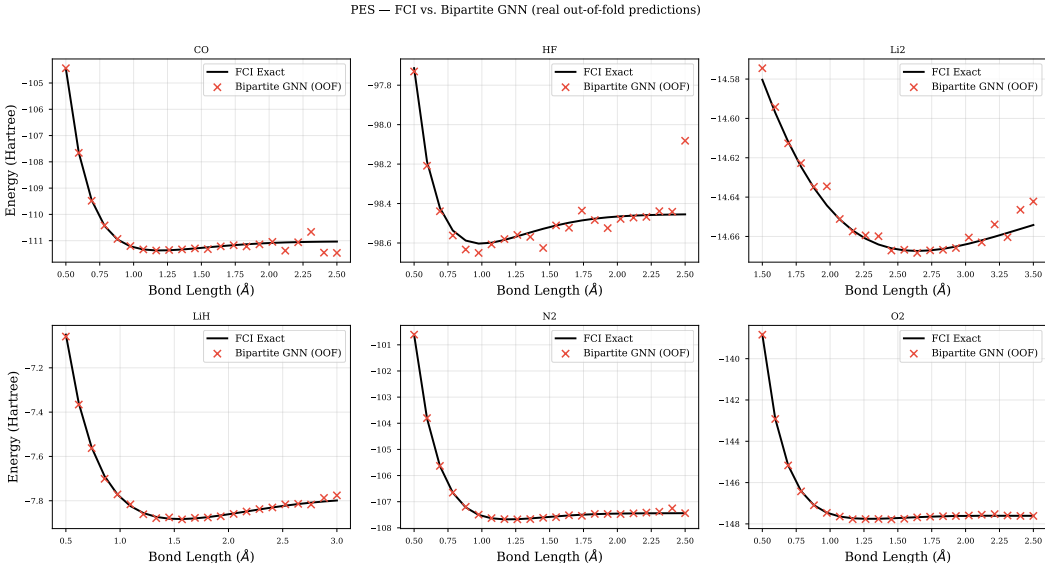


Figure 3: Potential energy surfaces for the six diatomic molecules. Solid lines represent FCI reference energies; crosses are genuine out-of-fold predictions of the bipartite GNN accumulated across all five CV folds. No prediction was produced by a model that had seen the corresponding geometry during training.

#### 5.4 Leave-One-Molecule-Out Transfer Analysis

To probe the representational boundaries of the model, we performed a leave-one-molecule-out (LOMO) validation, training on five species and evaluating zero-shot on the held-out molecule. Early stopping was performed on a validation split drawn from the *training* molecules; the held-out species was evaluated only once using the best checkpoint, ensuring no information from the test molecule influenced model selection.

Zero-shot MAE ranges from 0.040 Ha (LiH) to 0.161 Ha (Li<sub>2</sub>), a factor of four variation across species. The results are shown in Figure 4 and Table 2.

Contrary to a symmetry-based prediction in which homonuclear species (sharing inversion symmetry with the training molecules) would transfer most readily, the three homonuclear molecules span both extremes of the generalization spectrum: O<sub>2</sub> is mid-range (0.094 Ha) while N<sub>2</sub> (0.113 Ha) and Li<sub>2</sub> (0.161 Ha) exhibit the largest transfer errors. The simple  $\Delta Z$  correlation does not hold: Figure 4 shows no consistent trend with nuclear charge asymmetry.

Table 2: LOMO zero-shot MAE by held-out molecule.

Molecule	$\Delta Z =  Z_A - Z_B $	Zero-Shot MAE (Ha)
LiH	2	0.0401
HF	8	0.0785
O <sub>2</sub>	0	0.0945
CO	2	0.1074
N <sub>2</sub>	0	0.1130
Li <sub>2</sub>	0	0.1611

The data are better described by the orbital-structural similarity of the held-out species to the training distribution. LiH transfers most readily because both of its constituent atomic environments appear independently in the training set: lithium chemistry is represented by Li<sub>2</sub> and hydrogen chemistry by HF, giving the auxiliary nodes a prior over both atomic interaction vertices. Li<sub>2</sub>, by contrast, is the hardest case despite being homonuclear. Its bonding is dominated by the overlap of two diffuse 2s lithium orbitals, forming a weakly-bound  $\sigma$  system with no close structural analogue among the five training molecules (CO, HF, LiH, N<sub>2</sub>, O<sub>2</sub>), all of which involve tighter 2p orbital bonding or mixed-character  $\sigma$ - $\pi$  systems. The auxiliary node representations, trained entirely on these harder-bond chemistries, appear to encode an orbital-interaction prior that does not transfer well to the diffuse Li<sub>2</sub> case.

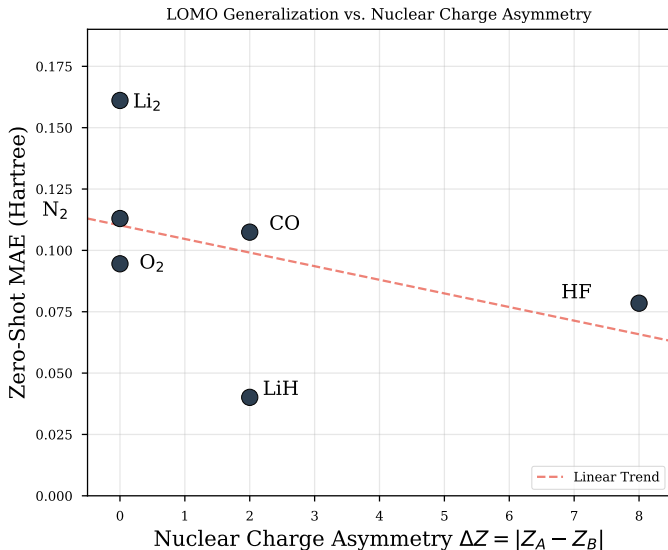


Figure 4: Zero-shot generalization error (LOMO-CV) as a function of nuclear charge asymmetry  $\Delta Z = |Z_A - Z_B|$ . The absence of a consistent monotonic trend indicates that  $\Delta Z$  alone does not explain transferability. LiH (low  $\Delta Z$ , low error) and Li<sub>2</sub> (zero  $\Delta Z$ , highest error) illustrate that the dominant factor is the orbital-structural dissimilarity of the held-out species from the training distribution.

## 5.5 Permutation Invariance

We verify that arbitrary permutation of the orbital indexing  $(p, q)$  within the  $h_{pq}$  and  $B_{pq}^L$  input tensors yields invariant energy predictions ( $|\Delta E| < 10^{-5}$  Ha). The test uses a physically valid symmetric Cholesky tensor ( $B_{pq}^L = B_{qp}^L$ ) consistent with the ERI supermatrix structure, confirming that the architecture preserves orbital-label parity.

## 6 Discussion

The performance advantage of the bipartite architecture stems from its structural consistency with the operator factorization. Standard node-to-node GNNs struggle to represent four-index tensors without combinatorial scaling; by defining the auxiliary Cholesky basis functions as explicit graph nodes, the architecture processes pairwise orbital correlation in a manner consistent with the structure of the Coulomb metric, without ever materializing the  $\mathcal{O}(N^4)$  ERI.

The LOMO analysis reveals that transferability is governed by the orbital-structural similarity of the held-out molecule to the training distribution. Species whose constituent atomic interaction environments are represented in the training set—such as LiH, whose atomic building blocks appear separately in Li<sub>2</sub> and HF—transfer most readily. Species with qualitatively distinct bonding characters—such as Li<sub>2</sub>, whose diffuse  $\sigma$ -bonded 2s system has no close analogue in the training set—exhibit the largest zero-shot errors. This suggests that the auxiliary node representations learn an orbital-interaction prior that is anchored to the chemical diversity of the training molecules rather than to any single symmetry descriptor.

The 2.2 $\times$  degradation observed in the ablation study confirms that the bipartite message-passing pathway is responsible for the bulk of the predictive improvement, rather than the depth of the energy readout head or the choice of one-body node features alone.

## 7 Limitations

Our empirical validation is constrained to six diatomic molecules in a minimal STO-3G basis, which limits the diversity of orbital structures encountered during training. The current architecture relies on a single-reference Hartree-Fock reference (RHF or ROHF), precluding direct evaluation on strongly multi-reference systems or excited states. The DeepSets and Compressed Orbital GNN baselines in Table 1 are internally implemented reference configurations. The closest externally published result is the concurrent GNN<sub>G</sub> of Carrasquilla-Gomez and Vargas-Hernández [2025], which targets total FCI energy rather than correlation energy and reports a per-molecule MAE of  $\sim 0.55$  Ha on an 80/20 split over the same benchmark; our 5-fold OOF MAE of 0.0296 Ha on the  $\Delta$ -ML correlation target represents a  $\sim 15\times$  reduction in absolute error under a stricter evaluation protocol.

## 8 Conclusion

We present a bipartite graph neural network motivated by the tensor factorization of the molecular Hamiltonian. By preserving the Cholesky structure of the ERI tensor as explicit auxiliary graph nodes rather than compressing it into scalar edge features, the architecture achieves a substantial reduction in correlation energy prediction error while maintaining sub-cubic practical scaling. LOMO validation suggests that zero-shot generalization tracks orbital-structural similarity to the training distribution. Factorized operator representations may provide a general design principle for structuring geometric deep learning architectures in quantum chemistry, particularly as larger and more chemically diverse orbital datasets become available.

**Code Availability** All experiments, model code, and data generation scripts are available at <https://github.com/maestroK/bipartite-cholesky-gnn>.

## References

- Nelson HF Beebe and Jan Linderberg. Simplifications in the generation and transformation of two-electron integrals in molecular calculations. *International Journal of Quantum Chemistry*, 12(4):683–705, 1977. doi: 10.1002/qua.560120408.
- Ville Bergholm, Josh Izaac, Maria Schuld, Christian Gogolin, Shahnawaz Ahmed, Vishnu Ajith, M Sohaib Alam, Guillermo Alonso-Linaje, B AkashNarayanan, Ali Asadi, et al. PennyLane: Automatic differentiation of hybrid quantum-classical computations. *arXiv preprint arXiv:1811.04968*, 2022.

- Simon Blaschke and Stella Stopkowicz. Cholesky decomposition of complex two-electron integrals over giasos: Efficient mp2 computations for large molecules in strong magnetic fields. *The Journal of Chemical Physics*, 155(16):164115, 2021. doi: 10.1063/5.0076588.
- Juan Carrasquilla-Gomez and Rodrigo A. Vargas-Hernández. Graph neural networks on one- and two-body integrals for molecular energy prediction. In *Machine Learning and the Physical Sciences Workshop, NeurIPS 2025*, 2025. URL <https://openreview.net/forum?id=UOpupYpns>.
- Anders S Christensen, Lars A Bratholm, Felix A Faber, and O Anatole von Lilienfeld. FCHL revisited: Faster and more accurate quantum machine learning. *The Journal of Chemical Physics*, 152(4):044107, 2020. doi: 10.1063/1.5126701.
- Valerii Chuiko and Paul W Ayers. Predicting energy of the quantum system from one- and two-electron integrals using deep learning. *arXiv preprint arXiv:2504.03849*, 2025. doi: 10.48550/arXiv.2504.03849.
- Justin Gilmer, Samuel S Schoenholz, Patrick F Riley, Oriol Vinyals, and George E Dahl. Neural message passing for quantum chemistry. In *International conference on machine learning*, pages 1263–1272. PMLR, 2017.
- Henrik Koch, Alfredo Sánchez de Merás, and Thomas Bondo Pedersen. Reduced scaling in electronic structure calculations using Cholesky decompositions. *The Journal of Chemical Physics*, 118(21):9481–9484, 2003. doi: 10.1063/1.1578621.
- Thomas Bondo Pedersen, Francesco Aquilante, and Roland Lindh. Density fitting with auxiliary basis sets from Cholesky decompositions. *Theoretical Chemistry Accounts*, 124(1):1–10, 2009. doi: 10.1007/s00214-009-0608-y.
- Zhuoran Qiao, Matthew Welborn, Animashree Anandkumar, Frederick R Manby, and Thomas F Miller III. Orbnet: Deep learning for quantum chemistry using symmetry-adapted atomic-orbital features. *The Journal of Chemical Physics*, 153(12):124111, 2020. doi: 10.1063/5.0021955.
- Raghunathan Ramakrishnan, Pavlo O Dral, Matthias Rupp, and O Anatole von Lilienfeld. Big data meets quantum chemistry approximations: The  $\delta$ -machine learning approach. *Journal of Chemical Theory and Computation*, 11(5):2087–2096, 2015. doi: 10.1021/acs.jctc.5b00099.
- Kristof T Schütt, Huziel E Saucedo, Pieter-Jan Kindermans, Alexandre Tkatchenko, and Klaus-Robert Müller. Schnet: A continuous-filter convolutional neural network for modeling quantum interactions. *The Journal of Chemical Physics*, 148(24):241722, 2018. doi: 10.1063/1.5019779.
- Kristof T Schütt, Michael Gastegger, Alexandre Tkatchenko, Klaus-Robert Müller, and Reinhard J Maurer. Unifying machine learning and quantum chemistry with a deep neural network for molecular wavefunctions. *Nature Communications*, 10(1):5024, 2019. doi: 10.1038/s41467-019-12875-2.
- Matthew Welborn, Lixue Cheng, and Thomas F Miller III. Transferability in machine learning for electronic structure via the molecular orbital basis. *Journal of Chemical Theory and Computation*, 14(9):4772–4779, 2018. doi: 10.1021/acs.jctc.8b00636.
- Shuo Zhang, Yang Liu, and Lei Xie. A universal framework for accurate and efficient geometric deep learning of molecular systems. *Scientific Reports*, 13(1):19171, 2023. doi: 10.1038/s41598-023-46382-8.

## A Extended Mathematical Formulation

This appendix details the theoretical mappings connecting the quantum many-body Hamiltonian to the factorized bipartite graph architecture, as well as the formal tensor operations comprising the message-passing framework.

### A.1 The Coulomb Metric and Positive Semi-Definiteness

The non-relativistic electronic Hamiltonian in second quantization is defined as:

$$\hat{H} = \sum_{pq} h_{pq} \hat{a}_p^\dagger \hat{a}_q + \frac{1}{2} \sum_{pqrs} g_{pqrs} \hat{a}_p^\dagger \hat{a}_q^\dagger \hat{a}_r \hat{a}_s \quad (1)$$

where  $h_{pq}$  represents the one-body core Hamiltonian and  $g_{pqrs}$  the two-electron repulsion integrals (ERI). The ERI tensor evaluates the Coulomb interaction between two orbital pair densities:

$$g_{pqrs} = \iint \phi_p^*(\mathbf{r}_1) \phi_q(\mathbf{r}_1) \frac{1}{|\mathbf{r}_1 - \mathbf{r}_2|} \phi_r^*(\mathbf{r}_2) \phi_s(\mathbf{r}_2) d\mathbf{r}_1 d\mathbf{r}_2 \quad (2)$$

By defining a composite index mapping  $I = (pq)$  and  $J = (rs)$ , the four-index ERI tensor can be flattened into a symmetric supermatrix  $G_{IJ} \equiv g_{pqrs}$ . The ERI supermatrix induced by the Coulomb kernel is positive semi-definite (PSD).

### A.2 Cholesky Factorization of the Interaction Vertex

The PSD nature of  $\mathbf{G}$  guarantees the existence of a Cholesky decomposition. We compute the incomplete Cholesky factorization  $\mathbf{G} \approx \mathbf{L}\mathbf{L}^T$ , subject to a truncation tolerance  $\epsilon$ :

$$G_{IJ} \approx \sum_{L=1}^{N_{aux}} L_{I,L} L_{J,L} \quad (3)$$

where  $\mathbf{L}$  is lower-triangular of dimension  $N^2 \times N_{aux}$ . Restoring the composite index  $I = (pq)$  defines the three-index Cholesky tensor  $B_{pq}^L \equiv L_{(pq),L}$ , recovering:

$$g_{pqrs} \approx \sum_{L=1}^{N_{aux}} B_{pq}^L B_{rs}^L \quad (4)$$

This factorization reduces the structural dimension of the interaction space from  $\mathcal{O}(N^4)$  to  $\mathcal{O}(N^2 N_{aux})$ . Because linear dependencies in the auxiliary basis scale approximately as  $N_{aux} \sim N$  in practice [Koch et al., 2003], the theoretical scaling is broadly bounded by  $\mathcal{O}(N^3)$ .

### A.3 Tensor Algebra of Bipartite Message Passing

Let  $\mathbf{x}_p^{(t)} \in \mathbb{R}^H$  be the latent representation of orbital node  $p$  at layer  $t$ , and  $\mathbf{h}_L^{(t)} \in \mathbb{R}^H$  the representation of auxiliary node  $L$ . Initial features are  $\mathbf{x}_p^{(0)} = [h_{pp}, \|h_p\|_2] \mathbf{W}_{emb}$  and  $\mathbf{h}_L^{(0)} = \mathbf{0}$ .

The Orbital-to-Auxiliary message aggregates pairs of orbitals through interaction channel  $L$ :

$$\mathbf{m}_L^{(t)} = \sum_{p=1}^N \sum_{q=1}^N B_{pq}^L \left( \mathbf{x}_p^{(t)} \odot \mathbf{x}_q^{(t)} \right) \quad (5)$$

where  $\odot$  denotes the element-wise Hadamard product in feature dimension  $H$ . Note that this is equivalent to the outer-product formulation  $\phi(\mathbf{x}_p, \mathbf{x}_q)$  in the main text; the summation contracts the orbital indices while preserving the feature dimension. Auxiliary node states are updated via:

$$\mathbf{h}_L^{(t+1)} = \mathbf{h}_L^{(t)} + \sigma \left( \mathbf{W}_A^{(t)} \mathbf{m}_L^{(t)} \right) \quad (6)$$

The Auxiliary-to-Orbital message broadcasts auxiliary states back:

$$\mathbf{m}_p^{(t)} = \sum_{L=1}^{N_{aux}} \sum_{q=1}^N B_{pq}^L \left( \mathbf{h}_L^{(t+1)} \odot \mathbf{x}_q^{(t)} \right) \quad (7)$$

Orbital states are residually updated:

$$\mathbf{x}_p^{(t+1)} = \mathbf{x}_p^{(t)} + \sigma\left(\mathbf{W}_O^{(t)} \mathbf{m}_p^{(t)}\right) \quad (8)$$

By executing Equations (5)–(8) via dense einsum tensor contractions, the architecture circumvents explicit allocation of an  $\mathcal{O}(N^4)$  edge adjacency matrix.

## B Justification of the $\Delta$ -Machine Learning Formulation

Predicting the absolute total energy  $E_{FCI}$  using a single scalar output exposes the network to a severe energy-scale imbalance. The total energy decomposes as  $E_{FCI} = E_{HF} + \Delta E_{corr}$ . In our dataset, the variance of  $E_{FCI}$  across six disparate molecular species spans  $\mathcal{O}(10^2)$  Hartree (from  $-7.8$  Ha for LiH to  $-148$  Ha for  $O_2$ ), while  $\Delta E_{corr}$  spans only  $\mathcal{O}(10^{-1})$  Hartree. Because the input graph uses strictly electronic integrals ( $h_{pq}, B_{pq}^L$ ), predicting  $E_{FCI}$  requires the network to implicitly reconstruct the nuclear repulsion  $V_{nn}$  from orbital features alone, dominating the gradient and masking the many-body objective. By adopting  $\Delta$ -ML [Ramakrishnan et al., 2015] and defining the loss on  $\Delta E_{corr}$ , we isolate the objective to the many-body scattering processes parameterized by the auxiliary interaction nodes.